Supplementary Material: Chirality routing non-polaritonic vacuum correlations in Landau polaritons

Ayoub El-Amrani,[1,*] Zakaria Mzaouali,[2,3] Houssam Sabri,[1]
Herschel Rabitz,[4] Abdelouahed El Fatimy,[1] and Dukhyung Lee[1,†]

[1]*College of Physical Sciences and Engineering, University Mohammed VI Polytechnic, Ben Guerir, 43150, Morocco.*
[2]*Jülich Supercomputing Centre, Institute for Advanced Simulation, Forschungszentrum Jülich, Wilhelm-Johnen-Straße, Jülich, 52428, Germany.*
[3]*Institut für Theoretische Physik, Universität Tübingen, Auf der Morgenstelle 14, 72076 Tübingen, Germany.*
[4]*Department of Chemistry, Princeton University, Princeton, New Jersey 08544, USA.*

SUPPLEMENTARY NOTE 1: MODEL, BASIS, AND NUMERICAL PARAMETERS

We summarizes the model conventions and numerical parameters used throughout the calculations. The goal is to make explicit the bare mode basis, the chiral active block used for the Bogoliubov diagonalization, and the experimentally extracted parameter set used to generate the figures in the main text. The calculations are based on the multimode Hopfield Hamiltonian (Eq. 7 in the main text). The bare mode basis is

$$\boldsymbol{a} = (a_+, a_-, b, c_1, c_3)^T , \tag{1}$$

where $a_\pm$ are the two circular cavity polarizations, b is the cyclotron resonance mode, and c_1, c_3 are the finite momentum magnetoplasmon modes selected by the cavity geometry.

The active chiral block is written in the basis

$$\boldsymbol{\eta}_- = \left(a_+, a_-^\dagger, b, c_1, c_3\right)^T . \tag{2}$$

In this basis, the dynamical matrix is

$$M_-(B) = \begin{pmatrix} \omega_0 + D & D & -i\bar{g}_{\mathrm{CR}} & -i\bar{g}_1 & -i\bar{g}_3 \\ -D & -\omega_0 - D & i\bar{g}_{\mathrm{CR}} & i\bar{g}_1 & i\bar{g}_3 \\ i\bar{g}_{\mathrm{CR}} & i\bar{g}_{\mathrm{CR}} & \omega_c & 0 & 0 \\ i\bar{g}_1 & i\bar{g}_1 & 0 & \omega_{\mathrm{MP},1} & 0 \\ i\bar{g}_3 & i\bar{g}_3 & 0 & 0 & \omega_{\mathrm{MP},3} \end{pmatrix} . \tag{3}$$

The bare dispersions are

$$\omega_c(B) = \frac{eB}{m^*}, \tag{4}$$

and

$$\omega_{\mathrm{MP},n}(B) = \sqrt{\omega_{p,n}^2 + \omega_c^2(B)}. \tag{5}$$

The couplings are

$$\bar{g}_{\mathrm{CR}}(B) = g_{\mathrm{CR}}\sqrt{\frac{\omega_c(B)}{\omega_0}}, \qquad \bar{g}_n(B) = g_n\sqrt{\frac{\omega_{\mathrm{MP},n}(B)}{\omega_0}}. \tag{6}$$

The diamagnetic coefficient is

$$D(B) = \frac{\bar{g}_{\mathrm{CR}}^2}{\omega_c} + \sum_{n=1,3} \frac{\bar{g}_n^2}{\omega_{\mathrm{MP},n}}. \tag{7}$$

The numerical parameters used in the calculations are summarized in Table I. They are taken from the experimentally fitted multimode Landau polariton model of Ref. [1].

TABLE I: Numerical parameters used throughout the calculations.

Quantity	Value	Meaning
$\omega_0/2\pi$	$0.925\,\mathrm{THz}$	Bare cavity frequency
m^*	$0.076m_0$	Effective mass
B_{CR}	$2.51\,\mathrm{T}$	CR–cavity zero detuning
B_{MP1}	$2.18\,\mathrm{T}$	MP_1–cavity zero detuning
B_{MP3}	$1.25\,\mathrm{T}$	MP_3–cavity zero detuning
g_{CR}/ω_0	0.18	CR coupling strength
$g_{\mathrm{MP1}}/\omega_0$	0.084	MP_1 coupling strength
$g_{\mathrm{MP3}}/\omega_0$	0.084	MP_3 coupling strength

TABLE II: Bogoliubov consistency checks. The table reports the maximum deviation over the full magnetic field range.

Quantity	Maximum deviation	Field position
$\|WW^\dagger - YY^\dagger - I\|_{\mathrm{F}}$	2.352×10^{-14}	$3.6190\,\mathrm{T}$
$\max\|WW^\dagger - YY^\dagger - I\|$	1.658×10^{-14}	$3.6190\,\mathrm{T}$
$\|WY^T - YW^T\|_{\mathrm{F}}$	1.273×10^{-15}	$0.2262\,\mathrm{T}$
$\max\|WY^T - YW^T\|$	7.425×10^{-16}	$0.2074\,\mathrm{T}$
$\|W^\dagger W - Y^T Y^* - I\|_{\mathrm{F}}$	2.348×10^{-14}	$3.6190\,\mathrm{T}$
$\max\|W^\dagger W - Y^T Y^* - I\|$	1.488×10^{-14}	$3.6190\,\mathrm{T}$
$\|W^\dagger Y - Y^T W^*\|_{\mathrm{F}}$	2.200×10^{-15}	$3.9939\,\mathrm{T}$
$\max\|W^\dagger Y - Y^T W^*\|$	1.478×10^{-15}	$3.9939\,\mathrm{T}$

SUPPLEMENTARY NOTE 2: BOGOLIUBOV CONSISTENCY AND COVARIANCE MATRIX PHYSICALITY

Here we document the internal consistency checks of the bosonic Bogoliubov transformation and the physicality checks of the Gaussian covariance matrix. These tests ensure that the numerical diagonalization preserves bosonic commutation relations and produces physical covariance matrices throughout the magnetic field scan.

Bogoliubov transformation. The Hamiltonian (Eq. 7 in the main text), is diagonalized by a bosonic Bogoliubov transformation,

$$P_\nu = \sum_i \left(W_{\nu i} a_i + Y_{\nu i} a_i^\dagger \right), \tag{8}$$

where ν labels the positive frequency normal modes and i labels the bare modes. With the row-wise numerical convention used here, preservation of bosonic commutation relations requires [2]

$$WW^\dagger - YY^\dagger = I, \tag{9}$$

and

$$WY^T - YW^T = 0. \tag{10}$$

The corresponding inverse completeness checks are

$$W^\dagger W - Y^T Y^* = I, \tag{11}$$

and

$$W^\dagger Y - Y^T W^* = 0. \tag{12}$$

The first pair of equations verifies that the normal mode operators are canonical bosons, while the second pair verifies completeness of the inverse transformation back to the bare cavity-matter operators.

The matrix residuals are quantified using both the Frobenius norm,

$$\|R\|_{\mathrm{F}} = \sqrt{\mathrm{Tr}(R^\dagger R)}, \tag{13}$$

and the maximum absolute matrix element $\max_{ij} |R_{ij}|$. The maximum deviations over the full magnetic field scan are given in Table II. All errors remain at the level of double precision numerical roundoff.

Covariance matrix. The covariance matrix is constructed from the quadrature vector

$$\boldsymbol{R} = (q_1, \ldots, q_N, p_1, \ldots, p_N)^T, \tag{14}$$

with

$$q_i = \frac{a_i + a_i^\dagger}{\sqrt{2}}, \qquad p_i = \frac{a_i - a_i^\dagger}{i\sqrt{2}}. \tag{15}$$

The covariance matrix is

$$V_{ij} = \frac{1}{2}\langle R_i R_j + R_j R_i \rangle. \tag{16}$$

In this convention the vacuum covariance is $V_{\text{vac}} = I/2$.

A physical Gaussian covariance matrix must satisfy [3]

$$V + \frac{i}{2}\Omega \geq 0, \tag{17}$$

where

$$\Omega = \begin{pmatrix} 0 & I \\ -I & 0 \end{pmatrix}. \tag{18}$$

Equivalently, all symplectic eigenvalues must satisfy

$$\nu_k \geq \frac{1}{2}. \tag{19}$$

Table III shows that the covariance matrices of the total ground state and the reduced four-mode state satisfy the condition 17, therefore, they are both physical.

TABLE III: Covariance matrix physicality checks.

State	$\min_{B,k} \nu_k$	$\min_B \lambda_{\min}(V + i\Omega/2)$
$\|GS\rangle$	0.500	-7.258×10^{-16}
$\rho_{a_-,\mathrm{CR},\mathrm{MP}_1,\mathrm{MP}_3}$	0.500	-6.891×10^{-16}

SUPPLEMENTARY NOTE 3: SPECTROSCOPIC SECTOR, PHOTONIC WEIGHTS, AND BROADENED VISIBILITY MAP

We detail here how the active sector polariton branches are obtained and how the transmission-like map used in the main text is constructed. The key point is that the map is not a full transfer matrix or input–output transmission calculation. It is a Lorentzian broadened photonic weight visibility proxy that visualizes the bright a_+-sector of the Hopfield model.

The positive frequency eigenvalues Ω_ν of the active chiral block define the polariton branches LP, UP_1, UP_2, and UP_3. For an active sector eigenvector

$$\boldsymbol{v}_\nu = \left(w_{\nu,a_+}, y_{\nu,a_-}, w_{\nu,\mathrm{CR}}, w_{\nu,\mathrm{MP1}}, w_{\nu,\mathrm{MP3}}\right)^T, \tag{20}$$

the a_+ photonic weight by branch is evaluated as

$$V_\nu = |w_{\nu,a_+}|^2 - |y_{\nu,a_+}|^2 = |w_{\nu,a_+}|^2. \tag{21}$$

Fig 1 shows a_+ net photonic weights V_ν, Eq. (21), by branch in the active spectroscopic sector. To obtain the transmission-like map, as shown in Fig. 2, each branch is broadened by a Lorentzian and weighted by its photonic content:

$$I(\omega, B) = \sum_{\nu \in \{\mathrm{LP},\mathrm{UP}_1,\mathrm{UP}_2,\mathrm{UP}_3\}} V_\nu(B) \frac{\Gamma_\nu}{[\omega - \Omega_\nu(B)]^2 + \Gamma_\nu^2}. \tag{22}$$

The final map is normalized by its maximum value,

$$\tilde{I}(\omega, B) = \frac{I(\omega, B)}{\max_{\omega,B} I(\omega, B)}. \tag{23}$$

The phenomenological broadening parameters used in the plots are

$$\Gamma_{\mathrm{LP}} = 0.10 \text{ THz}, \quad \Gamma_{\mathrm{UP}_1} = 0.085 \text{ THz}, \tag{24}$$

$$\Gamma_{\mathrm{UP}_2} = 0.065 \text{ THz}, \quad \Gamma_{\mathrm{UP}_3} = 0.10 \text{ THz}. \tag{25}$$

These parameters are chosen only to provide a visually smooth spectroscopic benchmark of the active sector branch structure.

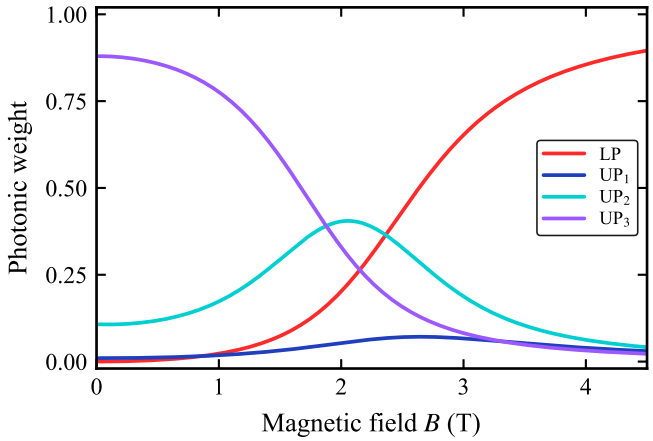

FIG. 1: Net photonic weights V_ν, Eq. (21), by branch. These weights quantify the spectroscopic visibility of the active polariton branches and provide the input weights for the broadened map.

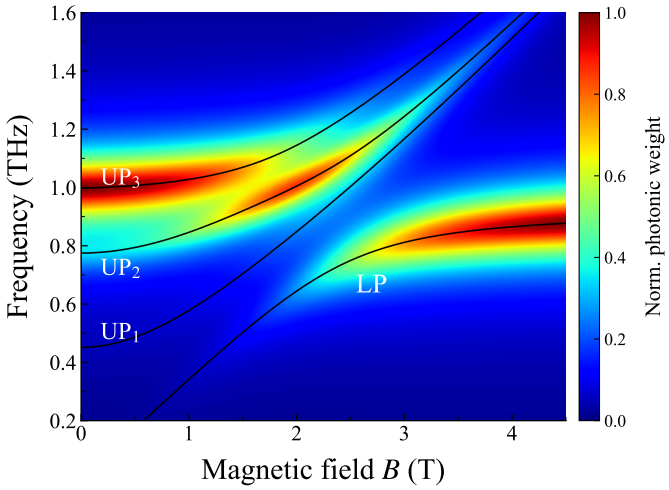

FIG. 2: Lorentzian broadened photonic weight map constructed using Eq. (22). The map is a phenomenological visibility proxy for the bright polariton branches and is not a full input–output transmission simulation.

SUPPLEMENTARY NOTE 4: NUMERICAL VERIFICATION OF THE CHIRAL SELECTION RULE

Here we verify the selection rule for anomalous correlators directly at the level of the ground state covariance matrix. The conserved chiral charge predicts that anomalous correlators with nonzero chiral charge vanish, while charge neutral anomalous channels may remain finite.

The conserved chiral charge is

$$Q = a_+^\dagger a_+ + \sum_j m_j^\dagger m_j - a_-^\dagger a_-, \tag{26}$$

where $m_j \in \{\mathrm{CR}, \mathrm{MP}_1, \mathrm{MP}_3\}$. Operators with nonzero Q charge have vanishing expectation values in a Q-eigenstate. Therefore,

$$\langle a_+ a_+ \rangle = 0, \qquad \langle a_+ m_j \rangle = 0, \tag{27}$$

whereas the a_--matter anomalous channels are allowed by symmetry, except for $\langle a_- a_- \rangle$.

The anomalous correlation matrix is obtained from the Bogoliubov coefficients as

$$\langle a_i a_j \rangle = -\sum_\nu w_{\nu,i}^* y_{\nu,j}. \tag{28}$$

The numerical results shown in Figure 3 confirm that all forbidden anomalous correlators remain at the numerical floor, while a_--matter channels, allowed by symmetry, are finite.

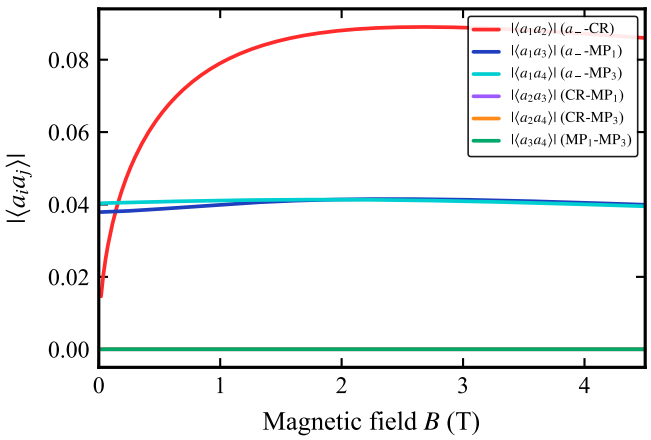

FIG. 3: Allowed anomalous correlators as a function of magnetic field. The dominant finite channels involve a_- and the matter modes, together with the allowed circular cavity anomalous channel.

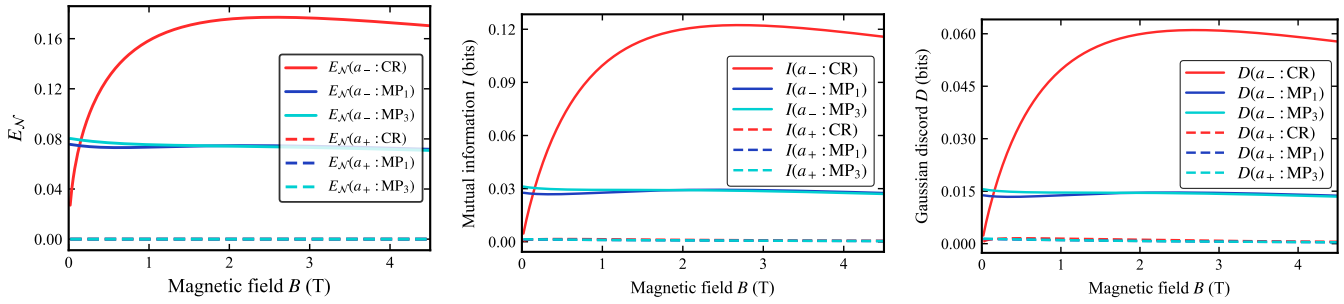

(a) **(b)** **(c)**

FIG. 4: Correlations between cavity polarizations and matter modes in the ground state. (a) Logarithmic negativity, Eq. (29); (b) mutual information, Eq. (30); and (c) Gaussian discord, Eq. (36). Solid curves correspond to correlations involving a_-, while dashed curves correspond to correlations involving a_+. Across all three measures, the a_- polarization carries the dominant cavity–matter correlation content, whereas correlations involving a_+ remain negligible or at the numerical floor. These results demonstrate a strong polarization selectivity of the correlated ground state and identify a_- as the cavity channel participating in the light–matter hybridization.

SUPPLEMENTARY NOTE 5: QUANTUM CORRELATION MEASURES

We introduce the three principal measures used throughout our analysis to characterize quantum correlations and information in the two mode ground state: logarithmic negativity, mutual information, and quantum discord. Together, these measures demonstrate that the spectroscopically active polarization mode a_+ remains effectively decoupled from the matter sector at the level of the ground state, while the dominant vacuum correlations are carried by the a_- channels.

To quantify bipartite entanglement, we employ the logarithmic negativity, which is based on the positive partial transpose (PPT) criterion [4, 5]. The logarithmic negativity across $A|B$ partition is computed from the symplectic eigenvalues $\tilde{\nu}_k$ of the partially transposed covariance matrix restricted to the bipartition,

$$E_\mathcal{N}(A:B) = \sum_k \max\{0, -\log(2\tilde{\nu}_k)\}. \tag{29}$$

In continuous variable systems, the partial transpose corresponds to flipping the sign of the momentum $(x, p) \to (x, -p)$ quadratures of subsystem B.

The quantum mutual information quantifies the total correlations between two subsystems:

$$I(A{:}B) = S(\rho_A) + S(\rho_B) - S(\rho_{AB}), \tag{30}$$

where $S(\rho)$ is the von Neumann entropy defined as:

$$S(\rho) = -\mathrm{Tr}(\rho \log_2(\rho)) \tag{31}$$

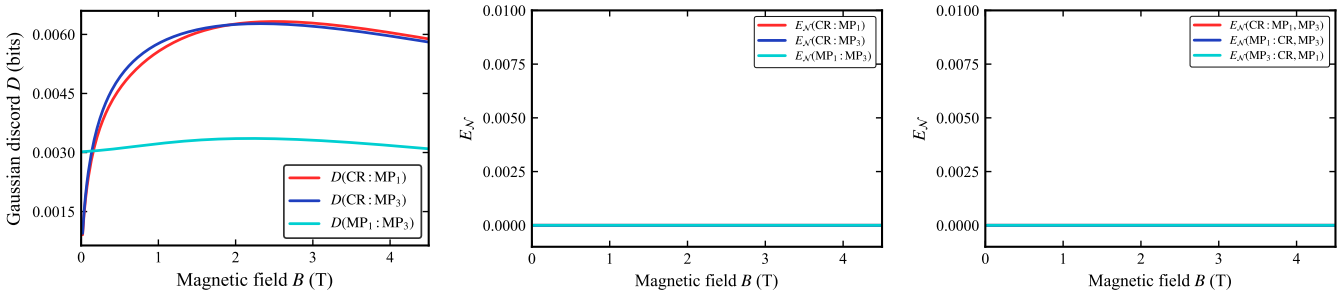

(a) **(b)** **(c)**

FIG. 5: Matter–matter correlations within the CR, MP_1, and MP_3 sector. (a) Gaussian discord between matter-mode pairs. (b) Pairwise logarithmic negativities for the $1|1$ cuts CR:MP_1, CR:MP_3, and MP_1:MP_3. (c) Matter-only $1|2$ logarithmic negativities for the cuts CR:$\{\mathrm{MP}_1, \mathrm{MP}_3\}$, MP_1:$\{\mathrm{CR}, \mathrm{MP}_3\}$, and MP_3:$\{\mathrm{CR}, \mathrm{MP}_1\}$. The finite discord in panel (a), together with the vanishing logarithmic negativities in panels (b) and (c), shows that the matter subsystem retains nonclassical Gaussian correlations without supporting either pairwise or matter-only multipartite entanglement.

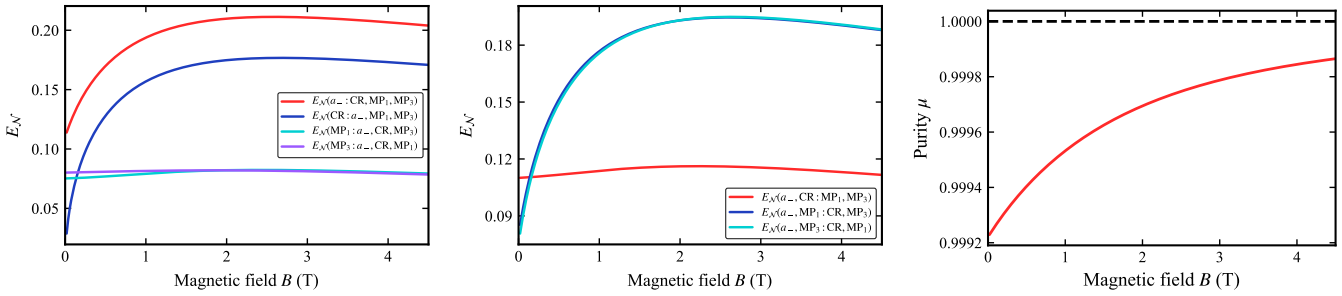

(a) **(b)** **(c)**

FIG. 6: Entanglement structure and purity of the reduced four mode subsystem $\{a_-, \mathrm{CR}, \mathrm{MP}_1, \mathrm{MP}_3\}$. (a) Logarithmic negativity, Eq. (29), across all $1|3$ bipartitions. (b) Logarithmic negativity, Eq. (29), across all $2|2$ bipartitions. (c) Purity, Eq. (38), of the reduced four mode state. The finite logarithmic negativities observed for both classes of bipartitions demonstrate that the cavity mode a_- is genuinely entangled with the collective matter sector across multiple partitions. Simultaneously, the purity remains close to unity over the entire parameter range, indicating that tracing out the inactive polarization a_+ introduces only negligible mixedness. Together, these results show that the essential quantum-correlated ground-state structure is faithfully captured by the nearly pure four mode subsystem, validating its use as an effective description of the light–matter entanglement.

In the multimode Hopfield system the subsystems A and B correspond to subsets of cavity or matter modes. Because the states are Gaussian, each entropy entering $I(A{:}B)$ is obtained from the symplectic eigenvalues ν_k of the corresponding reduced covariance matrix [3], such as:

$$S(\rho) = \sum_k h(\nu_k), \tag{32}$$

where the function $h(\nu)$ is given by:

$$h(\nu) = \left(\nu + \tfrac{1}{2}\right)\log_2\left(\nu + \tfrac{1}{2}\right) - \left(\nu - \tfrac{1}{2}\right)\log_2\left(\nu - \tfrac{1}{2}\right). \tag{33}$$

Since the quantum mutual information I captures total correlations, we will use quantum discord D to measure quantum correlations shared by the two subsystems A and B [6]. For pure states discord coincides with entanglement, but for mixed states captures quantum correlations shared even when the state is separable *i.e.* no entanglement. The quantum discord is defined as the mismatch between two quantities that are equivalent in the classical information theory:

$$D_{A\leftarrow B} = I(A{:}B) - J_{A\leftarrow B}, \tag{34}$$

where,

$$J_{A\leftarrow B} = S(\rho_A) - \inf_{\mathcal{M}_B\in\mathcal{G}} S(\rho_{A|\mathcal{M}_B}), \tag{35}$$

$\rho_{A|\mathcal{M}_B}$ is the conditional state of A when we measure B using a measurement $\mathcal{M}_B$ and $\mathcal{G}$ denotes the set of measurements on B which will be restricted to Gaussian ones, thus we will refer to it as Gaussian discord [7, 8]. Unlike the logarithmic negativity or the mutual information, the discord is not symmetric as it depends on the system upon which the measurement acts, therefore, we use the symmetrized Gaussian discord,

$$D(A:B) = \frac{1}{2}\left[D_{A\leftarrow B} + D_{B\leftarrow A}\right]. \tag{36}$$

Figures 4a, 4b and 4c demonstrate that a_+ is decoupled from the structure of the ground state, while a_- exhibiting finite correlations with all matter modes and through all measures.

As a result, the vanishing a_+-matter entanglement and the negligible a_+-matter mutual information and discord show that a_+ is effectively decoupled from the matter sector in the ground state correlation structure. This explains why tracing out a_+ introduces very little mixedness into the reduced $\{a_-, \mathrm{CR}, \mathrm{MP}_1, \mathrm{MP}_3\}$ sector. Furthermore, we establish that the matter subsystem alone does not contain pairwise or tripartite entanglement, even though it carries finite Gaussian discord as shown in Fig. 5a. This distinction is central to the interpretation of the cavity as mediating nonclassical but non-entangling matter correlations. For the three matter modes $\{\mathrm{CR}, \mathrm{MP}_1, \mathrm{MP}_3\}$, we test all pairwise $1|1$ cuts (Fig. 5b) and all $1|2$ bipartitions (Fig. 5c) using logarithmic negativity. The pairwise checks rule out direct two-mode matter entanglement. The $1|2$ cuts rule out tripartite entanglement within the matter subsystem. Thus, within the matter subsystem, the cavity-mediated correlations appear as Gaussian discord rather than entanglement. This supports the interpretation in the main text that the relevant correlated object is not a matter-only subsystem, but the collective a_--centered sector.

SUPPLEMENTARY NOTE 6: MULTIPARTITE ENTANGLEMENT, RESIDUAL PHOTONIC CORRELATIONS, AND PURITY

Here we analyze the reduced four mode subsystem

$$\mathcal{S}_4 = \{a_-, \mathrm{CR}, \mathrm{MP}_1, \mathrm{MP}_3\}. \tag{37}$$

The goal is to show that the dominant correlated sector is nearly isolated, effectively multipartite entangled, and only weakly mixed by the residual coupling to a_+. Fig. 6a and Fig. 6b show, respectively, that all inequivalent $1|3$ $2|2$ bipartitions exhibit robust inseparability, which that the reduced state of subsystem $\mathcal{S}_4$ fully inseparable.

For the reduced four mode state, the purity remains close to unity over the magnetic field range as shown in Fig. 6c, supporting the interpretation of the correlated subsystem as an approximately isolated Gaussian sector. Moreover, since the state of $\mathcal{S}_4$ is fully inseparable and taking its high purity, we can claim that the reduced four mode state effectively exhibits genuine multipartite entanglement [9]. The residual entanglement between the two circular cavity modes is small and decreases with magnetic field. This further supports the approximate factorization between the weakly connected active polarization and the dominant a_--centered correlated sector. The bipartition negativities, near-unity purity, and

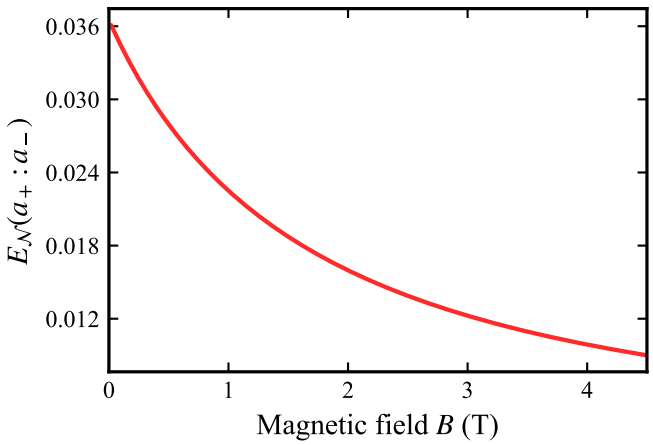

FIG. 7: Residual logarithmic negativity between the two cavity polarizations a_+ and a_-. The entanglement is small compared with the dominant a_--matter channels and decreases with magnetic field.

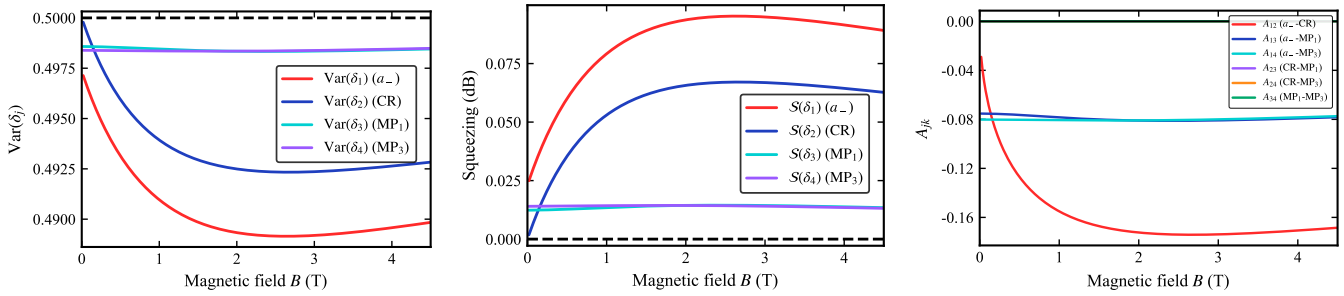

(a) **(b)** **(c)**

FIG. 8: Continuous variable graph-state diagnostics of the reduced four mode subsystem $\{a_-, \mathrm{CR}, \mathrm{MP}_1, \mathrm{MP}_3\}$. (a) Optimized nullifier variances, with the dashed line indicating the vacuum threshold $1/2$. (b) Corresponding nullifier squeezing, defined as $-10\log_{10}(2\,\mathrm{Var}\,\delta_j)$. (c) Off-diagonal elements of the effective adjacency matrix. The suppression of all optimized nullifier variances below the vacuum limit, together with the resulting positive squeezing, demonstrates the emergence of multipartite continuous-variable correlations characteristic of a Gaussian graph state. The extracted adjacency matrix reveals that these correlations are organized in a predominantly star-like topology, with the cavity mode a_- acting as the central hub and the strongest connection occurring along the a_-–CR link. These results identify the correlated ground state as a highly structured multimode Gaussian resource whose entanglement architecture is mediated by the active cavity polarization.

weak residual a_+-a_- entanglement (as shown in Fig. 7) show that $\mathcal{S}_4$ behaves as a nearly isolated a_--centered correlated sector of the full ground state. The purity of a Gaussian state with covariance matrix V is given by [3]:

$$\mu = \frac{1}{\sqrt{\det(2V)}}. \tag{38}$$

SUPPLEMENTARY NOTE 7: GAUSSIAN GRAPH-STATE DIAGNOSTICS

This note explains how the effective graph-state diagnostics used in the main text are obtained from the reduced covariance matrix. The purpose is not to claim an ideal infinitely squeezed cluster state, but to show that the nearly pure correlated sector has an organized Gaussian graph-like structure.

For the reduced subsystem $\mathcal{S}_4$, an effective continuous variable graph is obtained by minimizing the nullifier variances [10]

$$\delta_j = p_j - \sum_k A_{jk} q_k. \tag{39}$$

For a covariance matrix written in block form

$$V = \begin{pmatrix} V_{qq} & V_{qp} \\ V_{pq} & V_{pp} \end{pmatrix}, \tag{40}$$

the least-squares adjacency matrix is

$$A_{\mathrm{raw}} = V_{pq} V_{qq}^{-1}. \tag{41}$$

In the numerical implementation, the final reported adjacency matrix is symmetrized as

$$A = \frac{1}{2}\left(A_{\mathrm{raw}} + A_{\mathrm{raw}}^T\right). \tag{42}$$

The nullifier covariance matrix is

$$V_\delta = V_{pp} - A V_{qp} - V_{pq} A^T + A V_{qq} A^T. \tag{43}$$

The nullifier variances are the diagonal entries of V_δ.

Figure 8(a) shows the optimized nullifier variances of the reduced four mode subsystem. All variances remain below the vacuum threshold (1/2), indicating the presence of nontrivial collective quantum correlations among the modes. The same behavior is reflected in the corresponding nullifier squeezing shown in Fig. 8(b), where positive squeezing is obtained throughout the parameter range. Finally, Fig. 8(c) displays the off-diagonal elements of the effective adjacency matrix. The

dominant couplings connect the cavity mode (a_-) to the matter modes, with the strongest interaction occurring between (a_-) and CR. This structure indicates that the cavity mode acts as the main mediator of correlations within the reduced subsystem and gives rise to a predominantly star-like connectivity pattern.

* ayoub.el-amrani@um6p.ma
† dukhyung.lee@um6p.ma

[1] S. R. Endo, D. Kim, S. Liang, G. Lee, S. Kim, A. Covarrubias-Morales, M. Seo, M. J. Manfra, D. Lee, M. Bamba, and J. Kono, Cavity-mediated coupling between local and nonlocal modes in landau polaritons, Nanophotonics **14**, 4647 (2025).
[2] J. Colpa, Diagonalization of the quadratic boson hamiltonian, Physica A: Statistical Mechanics and its Applications **93**, 327 (1978).
[3] C. Weedbrook, S. Pirandola, R. García-Patrón, N. J. Cerf, T. C. Ralph, J. H. Shapiro, and S. Lloyd, Gaussian quantum information, Rev. Mod. Phys. **84**, 621 (2012).
[4] R. Simon, Peres-horodecki separability criterion for continuous variable systems, Phys. Rev. Lett. **84**, 2726 (2000).
[5] L.-M. Duan, G. Giedke, J. I. Cirac, and P. Zoller, Inseparability criterion for continuous variable systems, Phys. Rev. Lett. **84**, 2722 (2000).
[6] H. Ollivier and W. H. Zurek, Quantum discord: A measure of the quantumness of correlations, Phys. Rev. Lett. **88**, 017901 (2001).
[7] P. Giorda and M. G. A. Paris, Gaussian quantum discord, Phys. Rev. Lett. **105**, 020503 (2010).
[8] J. Eisert and M. B. Plenio, Introduction to the basics of entanglement theory in continuous-variable systems, Int. J. Quant. Inf. **1**, 479 (2003).
[9] O. Gühne and G. Tóth, Entanglement detection, Physics Reports **474**, 1 (2009).
[10] N. C. Menicucci, S. T. Flammia, and P. van Loock, Graphical calculus for gaussian pure states, Phys. Rev. A **83**, 042335 (2011).